STRONG ENVIRONMENTAL COUPLING IN A JOSEPHSON PARAMETRIC AMPLIFIER: SUPPLEMENTARY INFORMATION

LJPA Fabrication

The resonant circuit of the impedance transformed parametric amplifier (IMPA) is based on a previous experiment with lumped-element josephson parametric amplifiers (JPAs) coupled directly to a $50\,\Omega$ environment [1]. This design is shown in Fig. S1, along with a circuit diagram for the device. The circuit consists of 5 separate layers of optical lithography as well as a final e-beam lithography step to deposit the junctions. First, a base layer of 100 nm of aluminum was sputtered onto a sapphire substrate and patterned optically to form the bulk of the circuit. The insulator, 250 nm amorphous silicon (a-Si), was then deposited and patterned to create vias between the top wiring and base wiring layers. After an in-situ argon ion mill to remove the native oxide from the base layer to ensure good electrical contact between base and top wiring, a 100 nm of aluminum top-wiring was sputter deposited. The top wiring and insulator layers were then patterned and etched to form the parallel plate capacitor of the resonator and the crossovers. Finally e-beam lithography was used to pattern the junctions for the superconductin quantum interference device (SQUID), which were deposited using double angle evaporation and liftoff in an e-beam evaporator.

Taper Design

We chose a Klopfenstein taper [2, 3] to transform the impedance from $50\,\Omega$ to $15\,\Omega$ over a large bandwidth while minimizing the pass-band ripple. Given the $1\,\mu$m limitations of our optical lithography process, a taper consisting entirely of a $15\,\Omega$ co-planar wave-guide (CPW) transmission line would require a $200\,\mu$m center-trace with a $1\,\mu$m gap width. For a microstrip geometry we were contrained to a low impedance imposed by our thin a-Si dielectric, which would require a 100 nm trace width for a $50\,\Omega$ line. A hybrid CPW/microstrip transmission line shown in Fig. S2 was adopted for the taper where a $10\,\mu$m center trace and $5\,\mu$m gap CPW was shunted by a variable density of $2\,\mu$m wide microstrip sections. The result is a 20 mm long tapered transmission line designed for a maximum reflection of -20 dB above 4 GHz.

The microstrip part of this geometry was created using multi-layer crossovers as addi-

tional shunt capacitance. We tested this model using microwave finite-element simulations to ensure that the shunt capacitance behaved as expected, and to correct for the change in inductance imposed by the crossovers. After extensive simulation we found that using a small crossover width of $2\,\mu m$ and varying the density of crossovers provided the best control over impedance, as it allowed more evenly distributed shunt capacitance, prevented the inductance correction from becoming too large, and allowed the microstrip sections be applied uniformly over the meandered CPW.

Time Domain Reflectometry at milliKelvin temperatures

To verify that the profile of the taper followed the designed value, we employed time domain reflectometry (TDR) [4]. For this measurement, the time dependent reflection of a system is measured after the application of a fast step pulse, in order to measure the impedance of the system as a function of delay time, equivalent to the distance along the line. These measurements, shown in Fig. S3, were carried out in an adiabatic demagnetization refrigerator (ADR) with a base temperature of $\sim$55 mK to ensure the aluminum was superconducting, otherwise the loss from the normal aluminum CPW would overwhelm the
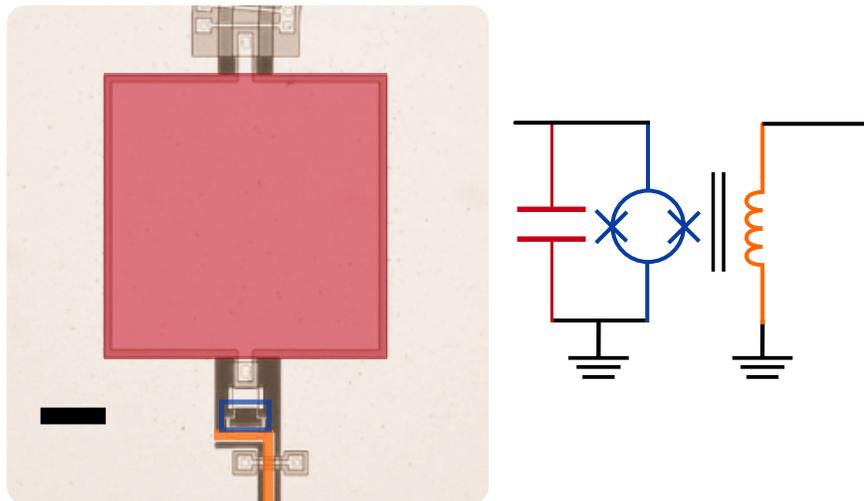

Figure S1. Optical micro-graph and circuit diagram of the lumped-element JPA design used in the IMPA. The device consists of a 4 pF parallel plate capacitor (red), in parallel with a $4\,\mu$A ciritical current SQUID loop (blue box). The pump tone and bias current are applied via an on-chip bias line (orange). The mutual inductance between the SQUID and bias line is 2.6 pH. Scalebar is $25\,\mu$m.
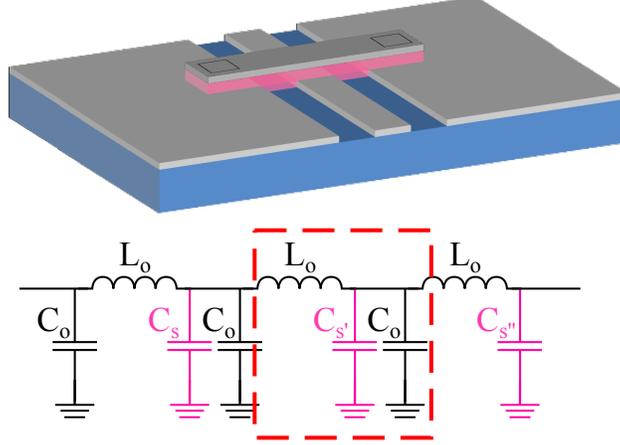
Figure S2. The hybrid CPW/microstrip geometry. To match of a wide range of impedances with features defined by photolithography, the CPW with 10-5 μm center trace-gap widths was shunted by a variable density of shunt capactitor crossovers. As the crossover width is much lower than a wavelength, the capacitance per unit-length of the transmission line smoothly increases, continuously reducing the characteristic impedance from 50 Ω to 15 Ω. A unit cell for this taper in the dashed red box, is shown above.

response TDR. All TDR data was taken using a Tektronix DSA8300 Digital Serial Analyzer with a 80E08B TDR/Sampling Module. The sampling module was connected directly to a CuNi line down to 4 K followed by a direct NbTi line down to the IMPA at 50 mK. Since the excitation voltage of this particular TDR sampling head is fixed, at 10 dB attenuator was applied to reduce the current at the device. The attenuated TDR data were calibrated using a 50 Ω terminator and an open at room temperature and corrected to obtain the proper impedances.

These TDR measurements were used to minimize reflections at the wire-bond due to excess inductance. As shown in Fig. S3 excess inductance in the wire-bonds of the signal line can lead to a large impedance mismatch at the start of the taper. This mismatch can lead to standing waves which severely limit the usable frequency range of the IMPA. It was only after greatly reducing the length of the wire-bonds from 1-1.5 mm to 0.3-0.5 mm that we observed the enhanced performance reported here.
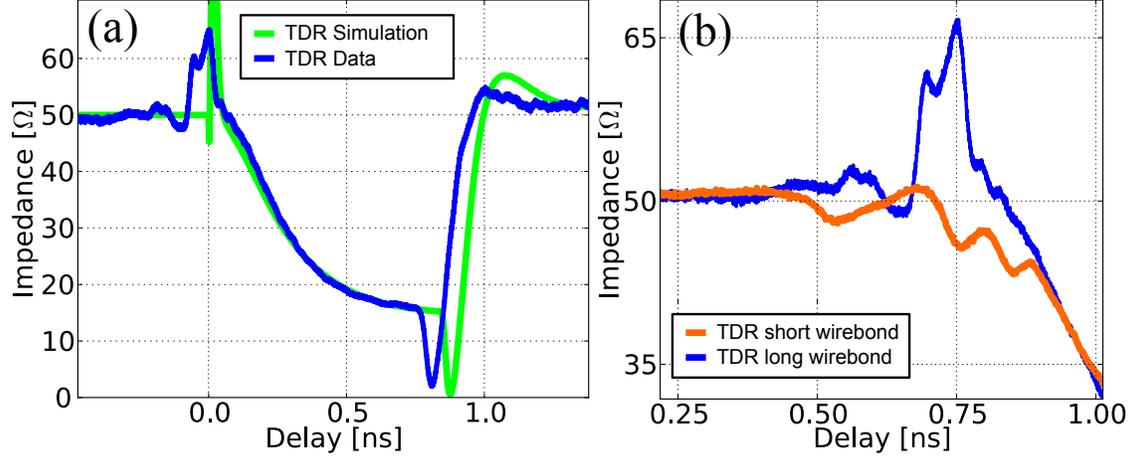
3

Figure S3. TDR analysis of an IMPA sample. (a) The TDR response of experiment (at 50 mK) *vs.* theory (SPICE simulations) of the IMPA. The tapered sections agree well. Both curves end in a dip followed by a jump in impedance, corresponding to the lumped element resonator. The peaks seen before the taper begins correspond to an impedance mismatch at the wire bond due to a large series inductance ~ 1 nH. This mismatch can lead to standing waves on the taper which limit IMPA performance. (b) An expanded view of the wire-bond mismatch for a sample with long (1-1.5 mm) vs short (0.3-0.5 mm) wire bonds. The improved wire bond mismatch is similar in magnitude to that of an SMA connector seen at 0.5 ns.

Pumpistor Model

To understand the non-Lorentzian gain peaks and enhanced bandwidth in the IMPA, one must properly model the interaction of the JPA with the frequency dependent impedance environment. Since this is a reflection amplifier, the gain can be calculated by the reflection coefficient at the interface between the external circuitry and the JPA. The frequency dependent impedance of the external circuit can be modeled straightforwardly using a SPICE model with the parameters shown in Fig. S4a. The tapered transmission line was modeled using 40 sections of equal delay transmission line corresponding to the impedance profile calculated using Ref. [3]. The mismatch due to the wire-bond was obtained using a section of transmission line at the input of the taper with a variable impedance and delay. The effect of the reflections due to the circulator was modeled using a resistor to ground whose value corresponds to the range of voltage standing wave ratio (VSWR) given by the manufacturer (Quinstar) specifications, at the end of a 50 Ω transmission line with variable delay.
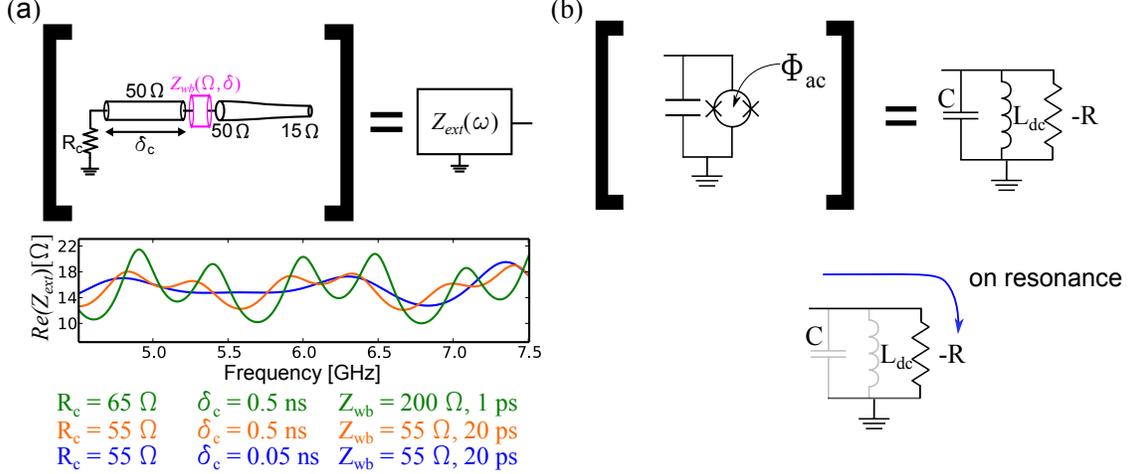
Figure S4. Simulated frequency dependent performance for the Pumpistor model. (a) The impedance of the external circuit was calculated using the LT SPICE software package. The taper, wirebond and distance between the IMPA and circulator were modeled using transmission line segments of variable impedance and delay. The magnitude of the reflection due to the circulator was modeled as a resistor to groud with a mis-match corresponding to the VSWR specification for the circulator. (b) The JPA can be modeled as a linear circuit element using the pumpistor model. This circuit can be approxmated as a parallel LC resonator shunted by a negative resistance. On resonance, the current through the JPA will be shunted through the negative resistance and the impedance will be given by the total real component $-R$.

The pumpistor model allows the flux-pumped SQUID to be treated as a linear cicuit component with the three inductances, given by Eqs. (1), (2), and (3) in the main text, where L_0 is the unbiased SQUID inductance in parallel with L_1 and L_2 which modify this bare inductance as pump power increases. To simplify the circuit analysis we express the effects of L_1 and L_2 as an equivalent parallel circuit with L_1' and L_2', such that L_1' modifies only the inductance of the circuit. Gain is introduce by the imaginary inductance of L_2' which behaves like a negative resistance, coupling power from the pump into the circuit. The parallel equivalent circuits are given by

$$Q_s = \frac{\omega_s L_1}{-i\omega_s L_2} = \frac{1}{\omega_i [L_j / \cos(\pi\phi_q/\phi_0)] Y_{\text{ext}}^*(\omega_i)}, \tag{1}$$

$$L_1' = L_1 \left(1 + 1/Q_s^2\right), \tag{2}$$

$$L_2' = L_2 \left(1 + Q_s^2\right). \tag{3}$$

For resonant circuits here we use $Q_s = Q \approx 3$, so $L_1' \sim L_1$ and $L_2' = \alpha L_2 \approx 10 L_2$ to keep
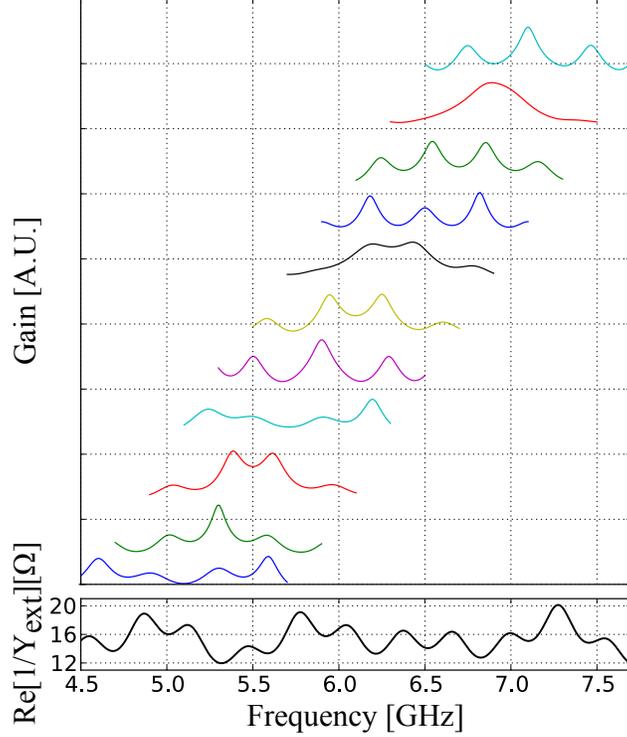
5

Figure S5. Additional simulations of the pumpistor model. Frequency dependence of the calculated gain profiles (each with a max gain approximately 20 dB) for Y_{ext} corresponding to the 10 cm cable length shown in Fig. 3(b) of the main paper. These calculated gain profiles are mostly symmetric, with regimes of single, multiple and broadened peaks, and show good qualitative agreement with the data. The vertical gridlines are spaced by 20 dB.

track of the series to parallel conversion. This allows us to write down an approximate circuit for the JPA shown in Fig. S4, where C is the shunt capacitance of the parallel plate capacitor of the lumped element JPA, L_c is an effective inductance including L_0 and L_1 for a given bias point and αL_2 gives a negative resistance in parallel. The circuit for these parallel admittances can be written as

$$Y_{\text{JPA}} = i\omega_s C + \frac{1}{i\omega L_c} - Y_R, \tag{4}$$

where Y_R is the magnitude of the JPA response given by:

$$Y_R = \frac{\pi^2 \sin^2(\pi\Phi_Q/\Phi_0)}{4\alpha\omega_s\omega_i L_{\text{j}}^2 Y_{\text{ext}}^*(\omega_i)} \left(\frac{\Phi_{ac}}{\Phi_0}\right)^2. \tag{5}$$
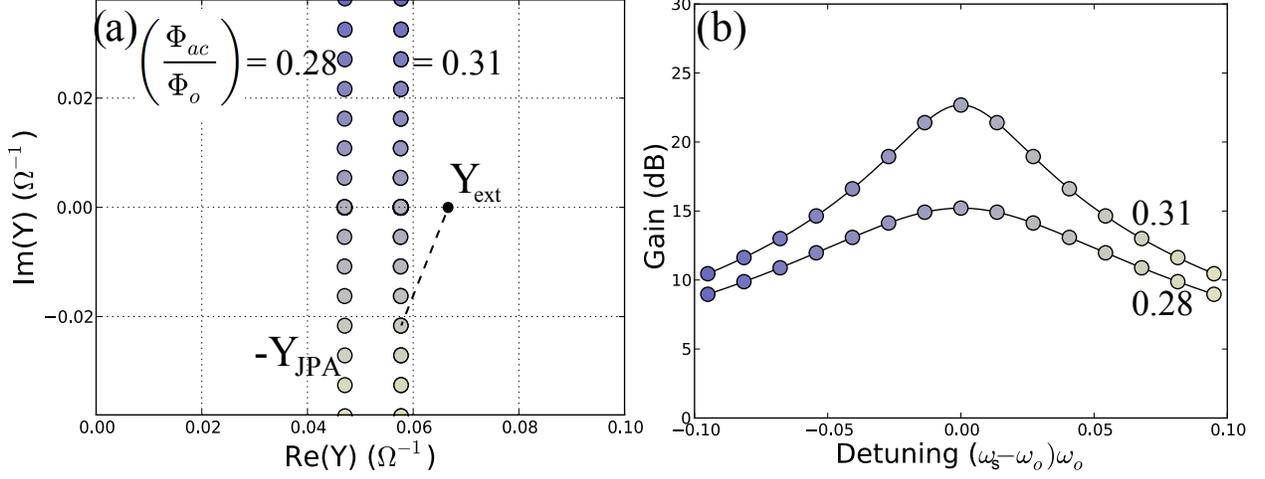
6

Figure S6. The frequency dependent behavior of $-Y_{\mathrm{JPA}}$ (open, colored circles) and Y_{ext} (black dot) in the complex plane. (a) For a constant Y_{ext}, Y_{JPA} is shown for two pump powers over a frequency range from $\omega_o - 0.1\omega_o$ to $\omega_o + 0.1\omega_o$ (each colored dot corresponds to a gain given in in panel (b)) where $\omega_o = \omega_p/2$. (b) The gain is inversely proportional to the distance between Y_{JPA} and Y_{ext} for a given frequency, indicated by the dashed line in (a). Since Y_{ext} is constant with frequency, the gain varies with the distance between the line given by Y_{JPA} and a point defined by Y_{ext}. The highest gain is found on resonance where Y_{JPA} is closest to Y_{ext}. The typical Lorenzian gain profiles are shown in (b) corresponding to the two different powers: $\Phi_{ac}/\Phi_o = 0.28$ and 0.31. Higher pump powers push $-Y_{\mathrm{JPA}}$ to the right; as it nears Y_{ext} the gain increases and bandwidth decreases.

Simplifying Eqs. (4) with $\omega_o^2 = 1/L_cC$:

$$Y_{\mathrm{JPA}} = \frac{1}{i\omega_s L_c}\left(1 - \frac{\omega_s^2}{\omega_o^2}\right) - Y_R \tag{6}$$

$$= \frac{1}{i\omega_s L_c}\frac{(\omega_o - \omega_s)(\omega_o + \omega_s)}{\omega_o^2} - Y_R. \tag{7}$$

With $\omega_o + \omega_s \approx 2\omega_o$, this yields Eqs. (5) from the main text.

This parallel to series conversion used to obtain Eq. (7) implicitly assumes Q_s is real. However, when a complex Y_{ext}^* is used to compute Q_s, the resulting correction to Y_{JPA} is negligible. It turns out the largest assumption in obtaining Eq. (7) is that $Q_s \approx 3$, a value constant in frequency. For this case α is predicted imprecisely over the narrow range of frequencies near resonance, as plotted in Fig. 3 of the main paper. However, α is simply a scaling factor for the pump power and Y_{ext}^*, both of which are not known precisely from experiment. These expressions are combined with the results of the SPICE model to obtain
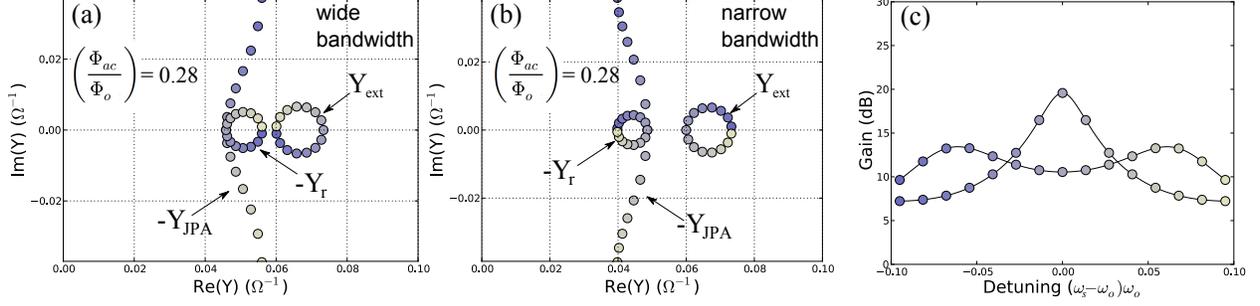
7

Figure S7. The frequency dependent behavior of $-Y_{\text{JPA}}, -Y_R$ and Y_{ext} in the complex plane for a sinusoidally varying Y_{ext}. The frequency at a given point, denoted by its color, each dot corresponds to a gain point shown in panel (c), where $\omega_o = \omega_p/2$. The gain at a given frequency is inversely propotional to the distance between $-Y_{\text{JPA}}$ and Y_{ext}. (a) In the wide bandwidth case, the profile Y_{JPA} nears Y_{ext} over a wider frequency range than otherwise. The resistive term reflects the variation in Y_{ext}, and displaces Y_{JPA}, providing a closer match to Y_{ext} over a broader range of frequencies than in Fig. S6. In the narrow bandwidth case (b) Y_{JPA} approaches Y_{ext} over a smaller range of freuqnencies. This happens when $\omega_p/2$ is located at a local minimum of Y_{ext}. The rolloff in gain with detuning is due to the imaginary portion of Eq. (7) growing with increased detuning. The corresponding gain profiles for (a) and (b) are shown in (c).

frequency dependent gain performance with good qualitative agreement to experiment as shown in Fig S5. Only with careful and very precise measurement of reflections in the microwave chain can one yield quantitative agreement with the exact formulation.

For additional insight into the engineering of large bandwidth, interaction between the terms $Y_{\text{ext}}, Y_{\text{JPA}}$ and $-Y_R$ (calculated using Eq. (7)) in the complex plane is shown in Figs. S6 and S7. The gain is inversely proportional to $|Y_{\text{ext}} + Y_{\text{JPA}}|$, equivalent to the distance between Y_{ext} and Y_{JPA}. By increasing pump power, $-Y_R$ increasingly deforms Y_{JPA}. Large bandwidth is achieved by minimizing the distance between Y_{JPA} and Y_{ext} over a larger range of frequencies. This is shown in contrast to the ideal case with no variation in Y_{ext}, which produces the typical Lorentzian gain profile.

"Pumpistor" predictions on saturation power

According to the "pumpistor" model for degenerate parametric amplification, saturation power depends directly on the ratio of signal amplitude to critical current and scales in-

versely with coupled Q. As bandwidth should also scale as $1/Q$ this would compensate an increase in amplified noise with a commensurate increase in saturation power. In the IMPA however, we see a much larger increase in bandwidth up to about 700 MHz. This large bandwidth exhibited at certain pump frequencies, might be a concern if the additional amplifier quantum fluctuations limit the saturation power. Considering the amplified quantum fluctuations at 6.7 GHz for 700 MHz of bandwidth and an average gain of 17.5 dB we have a total output power of

$$P_{out} = 10 * \log\left(\frac{6.7 * 10^9 * h * 7 * 10^8}{1 * 10^{-3}}\right) + 17.5 \approx -97.5 \, dBm \tag{8}$$

If we compare this to the average input saturation power for a coherent signal (-108 dBm) with the average gain 17.5 dB we get -90 dBm output saturation power. Previous LJPA devices with a coupled-Q of 10 have displayed input saturation values of -115 dBm at 20 dB of gain, giving an output saturation power of -95 dB [1]. Thus the increase in average output power is consistent with the expected 5 dB increase going from a coupled Q of 10 to a coupled Q of 3. By lowering the coupled Q and operating the device at a slightly lower gain, the amplified quantum fluctuations are 7.5 dB below the saturation power limit for a coherent signal.

Additional nonlinearities can arise in the gain vs. signal power curve either when the signal is significantly detuned from the pump or when a non-optimal pump power and flux value is chosen. In these cases the signal can act as a secondary input pump, which first causes the gain at the signal frequency to increase with signal power before saturating and compressing below the original level. While this effect can be calibrated for in single frequency measurements, it can cause distortion in broader band or pulsed signals. If the large bandwidth of our device was due to more complicated nonlinear dynamics it is a possible concern that certain regions of the 700 MHz span might display such non-ideal saturation behavior. We demonstrate in Fig. S8 a series of representative curves of transmission power (scaled to 0) vs. input signal power for various frequencies within the 700 MHz span. All curves other than (ix) demonstrate ideal linear behavior before saturation. In the case of curve (ix), a light upward deviation (0.2 dB above the background) occurs before the gain compresses. These curves are generally representative of the entire span, with small non ideal behavior confined to regions sections at the very edges. Far less ideal saturation power behavior is observed outside of this region, but only where the gain falls off sharply as
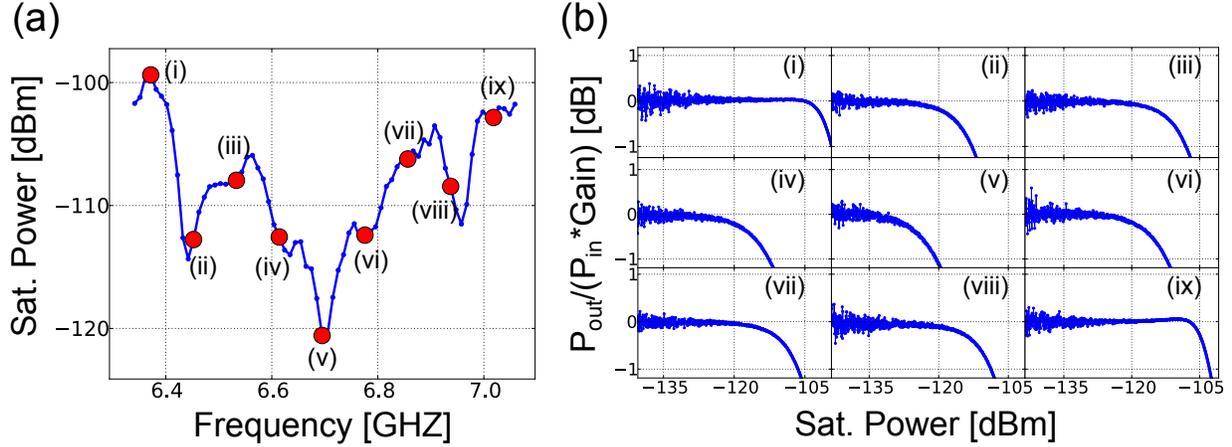
9

Figure S8. (a) Graph of saturation power vs. frequency from the main text. Large (red) dots are used to denote frequencies for which a full transmission power vs input signal power curve is shown. (b) Graphs of transmission power vs. input signal power for the points depicted in (a). Here the output power has been scaled by the low signal power limit, such that the ideal transmission is 0 and -1 denotes the 1 dB compression point. The first 8 graphs display an ideal linear dependence on power before saturating to -1 dB. The final graph at the edge of the amplified range displays a slight increase in gain, up by 0.2 dB, before saturating in the normal way. In general, this small upturn is only observed at the edge of the 700 MHz span.

expected.

Noise measurements

The Paramp system noise values displayed in this paper were calculated using the method of signal to noise ratio improvement [1, 5] discussed in the main text. In this method the amplified noise and transmission amplitude is first measured when the amplifier is turned off. The amplifier is then turned on and the amplified noise and transmission amplitude are once again measured. By comparing the increase in transmission power (gain) to the increase in amplified noise we can measure system noise amplified by the paramp provided we know the system noise amplified by thehigh electron-mobility transistor (HEMT) . In this measurement signal loss between the paramp and the HEMT can make this ratio seem smaller and must be taken into account when measuring the amplified HEMT noise. In our setup, shown in Fig. S9, we use a y-factor measurement [3] with a heated $50\,\Omega$ resistor
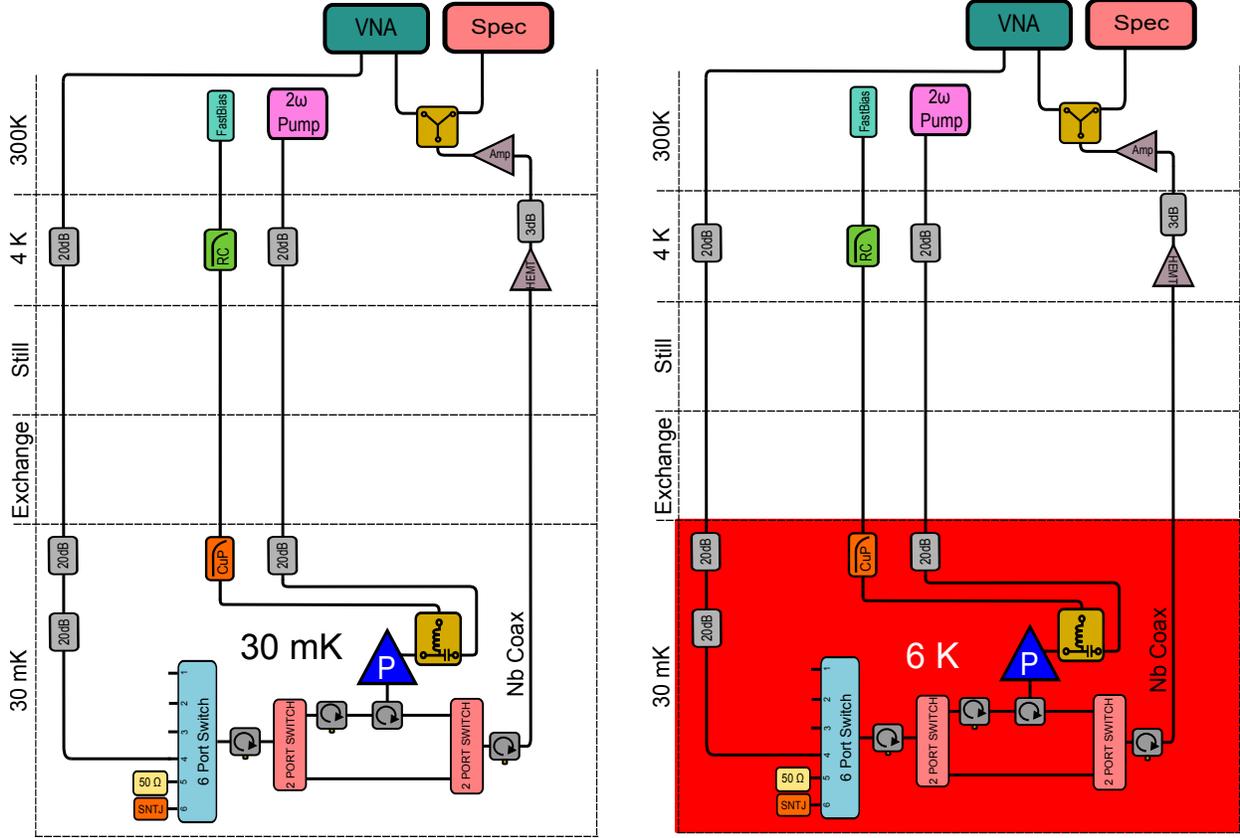
10

Figure S9. Schematic for paramp experimental setup used to characterize noise. The left figure shows the experimental setup with paramp, circulators, and microwave switches at base temperature. The $50\,\Omega$ on the 6 port switch is heated to calibrate the HEMT noise. The right schematic shows the portion of the fridge heated (red) to perform a y factor measurement. When this calibration is done the 2 port switches are are set to the straight through path which provides 2 circulator channels between the $50\,\Omega$ and the HEMT, the same number of circulators between the HEMT and signals amplified by the paramp. As circulators are the dominant source of loss, the HEMT system noise seen by the paramp and the $50\,\Omega$ should be equivalent.

on the cold plate of our refrigerator. In this setup both the $50\,\Omega$ resistor and the paramp are connected to the HEMT by copper microwave flex cables at $30\,\text{mK}$, 2 circulators, and a Nb coaxial cable connected between $30\,\text{mK}$ and the HEMT at $4\,\text{K}$. Due to the difficulty of heating just the $50\,\Omega$ resistor we use a method in which the entire cold plate of the refrigerator in heated to a much larger temperature ($6\,\text{K}$) and allowed to stabilize before a measurement is performed. The HEMT amplifier is on a different plate and its temperature is held steady over the course of this experiment. This methodology, while allowing for

11

accurate temperature measurement of the resistor, can mis-characterize the effect of loss between the resistor and the HEMT. Any dissipative loss coming from attenuation on the 30 mK plate would add noise to the signal as it was also at the higher 6 K temperature. We assume the dominant source of potential loss comes from the microwave circulators, as the superconducting and copper cables should have negligible loss at these temperatures. The circulator insertion loss was measured at room temperature to be between 0.5 and 0.3 dB. To account for this we have added 1 dB error bars to our measurement of the HEMT noise which are in turned scaled to give error bars for the signal to noise ratio improvement of the paramp.

[1] J. Mutus, T. White, E. Jeffrey, D. Sank, R. Barends, J. Bochmann, Y. Chen, Z. Chen, B. Chiaro, A. Dunsworth, et al., App. Phys. Lett. **103**, 122602 (2013).

[2] R. Klopfenstein, Proc. IRE **44**, 31 (1956).

[3] D. M. Pozar, *Microwave engineering* (John Wiley & Sons, 2009).

[4] R. H. Cole, Annual Review of Physical Chemistry **28**, 283 (1977).

[5] M. Hatridge, R. Vijay, D. Slichter, J. Clarke, and I. Siddiqi, Phys. Rev. B **83**, 134501 (2011).